

# Supersampled scanning transmission X-ray microscopy for high-resolution vibration-free imaging

Simone Finizio,\* Benjamin Watts, Benedikt Rösner, and Jörg Raabe

*Paul Scherrer Institut, 5232 Villigen PSI, Switzerland*

E-mail: [simone.finizio@psi.ch](mailto:simone.finizio@psi.ch)

## Abstract

Scanning transmission X-ray microscopy (STXM) is a nanoscale imaging technique that can utilize several powerful contrast mechanisms for the quantitative mapping of chemical and physical materials properties. Spatial resolutions down to 7 nm at the soft X-ray energy range have been demonstrated. A limiting factor for high-resolution STXM imaging is given by the positioning precision of the sample with respect to the focusing optic, with the current state-of-the-art leading to significant overheads, especially at low pixel dwell times, and being vulnerable to unavoidable external vibrations sources. In this work, we present a method, called *supersampled scanning microscopy* that allows for a significant reduction of overhead times while simultaneously removing the effects of vibrational noise by sampling the position of the sample at a rate significantly higher than the vibration spectrum and reconstructing the sample transmission image from the recorded list of positions and detector counts. We demonstrate the performance of the technique with a set of proof-of-concept high-resolution imaging experiments.

## Keywords

STXM, X-ray microscopy, High resolution imaging

In recent decades, third-generation synchrotron lightsources have provided bright photon beams with photon energies ranging from infrared to hard X-ray wavelengths. The availability of highly brilliant X-ray radiation has allowed for countless scientific discoveries in a wide range of fields. Recently, a new fourth-generation of synchrotron lightsources has been developed, and several of these new ring designs have been built, mostly by upgrading existing rings. This next generation is referred to as diffraction limited storage rings (DLSRs), and offers significant increases in the source brilliance and the coherent photon flux delivered to the beamlines of typically one to two orders of magnitude compared to third-generation sources depending on the lattice type, source properties, and photon energies. The impact is expected to revolutionize scientific investigations with synchrotron light in many fields.<sup>1,2</sup>

One portfolio of techniques that will profoundly benefit from the upgrade of synchrotron lightsources to DLSRs is X-ray microscopy, specifically photon-hungry techniques that require a high degree of coherent illumination such as nanofocus imaging or coherent diffractive imaging (CDI). A great example of the significant improvements offered by DLSRs is given by soft X-ray ptychography imaging, a CDI technique where the routine acquisition of high-resolution (sub-10 nm at the soft X-ray range) images was demonstrated.<sup>2-6</sup> Besides CDI, direct nanofocus imaging techniques, such as scanning transmission X-ray microscopy (STXM), will strongly benefit from the increased beam quality. This technique utilizes a diffractive X-ray lens (Fresnel zoneplate - FZP) to focus a monochromatic X-ray beam onto a nanometric spot. In the case of STXM, the beam is focused on the surface of an X-ray semi-transparent sample and an image is obtained by scanning the sample and recording the transmitted X-ray intensity for each point of the scan. Under a sufficiently coherent illumination of the FZP, the achievable spatial resolution is limited by the diameter of the Airy disk generated by the FZP: the size of the central spot is 1.22 times as large as the outermost zone width of the FZP. Whereas it helps to decrease the outermost zone width to

achieve higher microscopic resolution, two major limitations arise. One is the technological limitation of lithographic fabrication processes to produce the required FZP, and the other is the fact that high-resolution FZP usually suffer from decreasing diffraction efficiencies as volume effects kick in<sup>7</sup> and ever-smaller nanostructures also tend to be less perfect. The current soft X-ray STXM resolution record stands at 7 nm, achieved using a tailored zone-doubled Ir FZP.<sup>8</sup>

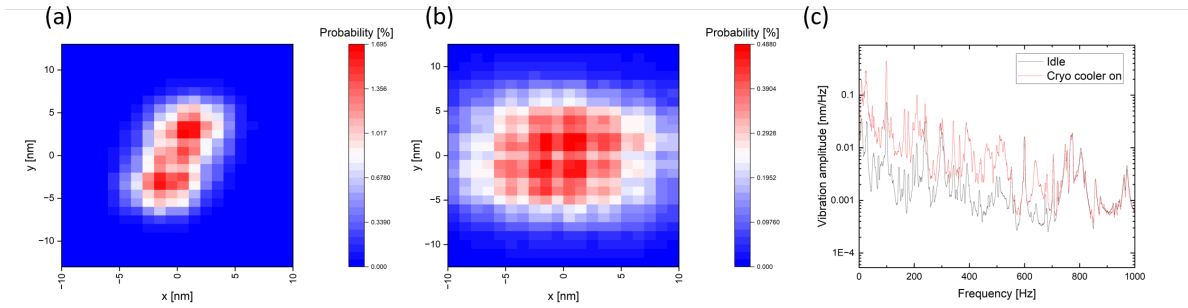


Figure 1: (a) Heatmap showing the sample positioning uncertainty in idling conditions (control loop attempting to keep position); (b) Same conditions as (a), but with a closed cycle cryostat, normally employed for cooling down samples, activated; (c) Spectrum of the vibrations in both configurations.

While the principle of sub-10 nm resolution soft X-ray STXM imaging has been demonstrated already in 2020,<sup>8</sup> its use in regular measurement campaigns has not been widespread, due to the combination of two preconditions: a relatively low efficiency of high-resolution FZP optics (as discussed above) and a very high positioning precision and stability. Further, the very short depth of focus of high resolution FZPs<sup>8</sup> means that the high positioning precision is required in all three spatial dimensions, although the level of precision required along the beam axis is still an order of magnitude less than the transverse precision requirements. When discussing positioning precision and stability, it is important to understand that the positioning stability does not need to be absolute, but relative to the time used to collect detector counts (i.e. the pixel dwell time). While DLSRs help to overcome the challenges for the focused beam size and the time required to collect sufficient photon counting statistics, this only solves half of the problem with high-resolution STXM imaging, as the reliable,

stable, and high precision positioning of the sample with respect to the FZP is very difficult to achieve with conventional approaches.

In routine STXM imaging, sample positioning is performed by means of a piezoelectric stage with an interferometric feedback system. At the PolLux endstation of the Swiss Light Source,<sup>9</sup> the interferometric metrology is performed by a dual pass heterodyne interferometer.<sup>10</sup> The difference between the recorded interferometer position and the desired position is then used in a proportional-integral-differential (PID) feedback loop to actuate the piezoelectric stage. This is performed using the Orocosp Project libraries<sup>11</sup> on a realtime Linux kernel, which is operated with a 2 kHz clock. However, even with a fully optimized feedback control system, perfect positioning at the nanoscale cannot be achieved, due to the presence of environmental vibrations that cannot be completely canceled out. These vibrations lead to an uncertainty on the position of the probing beam on the sample surface and can therefore remarkably reduce the quality of the recorded STXM images. Fig. 1(a) shows the uncertainty on the sample position when the control loop is attempting to maintain the user-defined set position. A  $1\sigma$  root mean square uncertainty of about 2.4 nm in the  $x$  axis and of 3.8 nm in the  $y$  axis can be observed. This is negligible for most applications of low-resolution imaging, where both spot size and scanning steps are much larger than the vibration amplitude, but it becomes relevant for high-resolution images when the X-ray spot size becomes comparable to the vibration amplitude. On top of this fundamental issue, the use of additional equipment in the endstation, such as e.g. a closed cycle cryostat used for sample cooling, can lead to a significant increase in the vibration amplitude (see Fig. 1(b), with a significantly higher  $1\sigma$  uncertainty of about 9.5 nm in the  $x$  axis and 12.7 nm in the  $y$  axis). By analyzing the spectrum of the vibrations (see Fig. 1(c)) it is possible to observe that several vibration modes are present, with the strongest at approximately 100 Hz for this setup. For other STXM endstations, the exact details of the positioning uncertainty and the vibrations' spectral content will vary, but the principle issue that environmental noise couples into the positioning will remain.

The PolLux STXM control system utilizes two scanning protocols: *point-by-point* (PP) and *constant velocity* (CV), also known as *line-at-once*. The PP mode changes the setpoint of the positioning control loop for each pixel of the scan and waits for the position to settle before it records the transmitted photon intensity (by integrating the signal for a user-defined dwell time). The PP mode is precise within the uncompensated vibration noise, but at the price of large overheads required for the settling of the sample position at each pixel, which limits the scan speed. The second scanning protocol, the CV mode, trades positioning precision for speed. In this mode, each line of the region of interest (ROI) is scanned with the piezoelectric stage moving at a constant velocity, which is defined by the number of pixels in the line and the required dwell time (calculated as  $v = d/(t_p N_p)$ ,  $d$  being the length of the line,  $t_p$  the pixel dwell time, and  $N_p$  the number of pixels in the line). The transmitted photon intensity is continuously recorded and separated in  $N_p$  bins, each with a  $t_p$  duration in time. As the piezoelectric stage cannot instantaneously accelerate to or decelerate from a non-negligible velocity, a region before and after the ROI is dedicated to the acceleration and deceleration of the stage. This acceleration distance is user-defined, and depends on parameters such as the velocity to achieve and the dimension of the ROI. The acceleration distance contributes to the otherwise negligible overhead of CV scans, as part of the measurement time will be spent in the acceleration/deceleration regions. Fig. 2 demonstrates the impact of the scanning protocol on the scanning overhead for an image, where the significant difference between the PP and the CV modes can be observed. The constant overhead weights more for shorter dwell times. With the increased brilliance of the source offered by DLSRs, shorter dwell times will become more common, and scanning overhead will therefore become more limiting under experimental conditions, which needs to be addressed.

In this work, we present a new STXM imaging protocol that allows for the combination of high-precision positioning for the acquisition of high-resolution images with negligible imaging overheads and the possibility to eliminate the effects of external vibrations. This

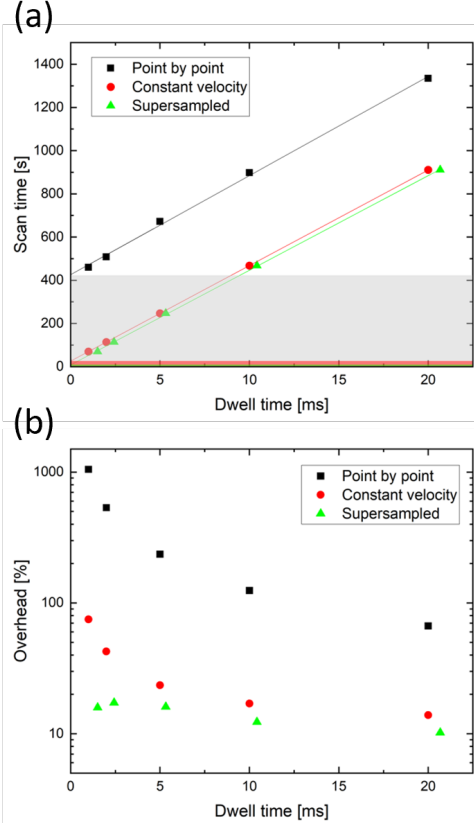


Figure 2: (a) Total scan time determined from STXM scans for a  $200 \times 200 \text{ px}^2$ ,  $2 \times 2 \mu\text{m}$  scan in the PP, CV, and with the supersampled configurations as a function of the desired pixel dwell time. (b) Corresponding scan overhead fraction (calculated as the ratio between the overhead time and the nominal scan time).

protocol is based on the principle that vibrations and positioning glitches can never be fully compensated for by conventional methods, but that they occur at timescales much longer than the interaction of the X-ray photons with the sample. By measuring the position of the sample at a rate faster than the mechanical vibrations, the true position at which the photon interacts with the sample can be determined with much higher precision and accounted for in the image reconstruction. In this way, unpredictable vibrations and positioning glitches simply become part of the scanning motions. In addition, this relaxes the need to achieve precise sample positions (as long as a sufficiently uniform coverage of the ROI can be provided), allowing for an increase in the scanning velocity to the physical limits of the stages.

The setup described in this work is sketched in Fig. 3(a). The position of the sample

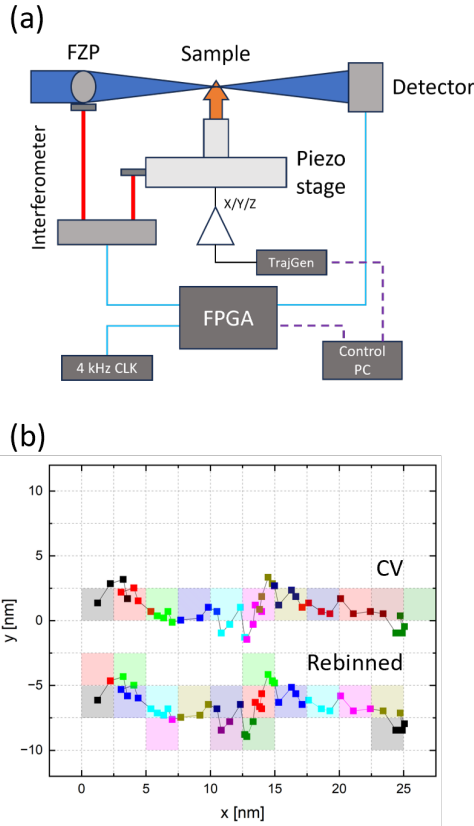


Figure 3: (a) Sketch of the setup employed for the supersampled scanning microscopy measurements. The position of the sample, together with the detected photon counts, is recorded at a fast (4 kHz) rate by a dedicated FPGA setup. The piezoelectric stage is scanned with minimal positioning precision requirements using a trajectory generator integrated within the Orocospo positioning system of the endstation. (b) Sketch of the operation principle of the CV mode and of the principle of supersampled imaging for the same scan trajectory. In supersampled imaging, the data is assigned to a pixel based on the recorded position, allowing one to overcome possible artifacts caused by vibrations or glitches in the positioning system.

with respect to the FZP is measured by means of a dual pass heterodyne interferometer, as described above. This interferometer can be sampled up to about 770 kSa/s. In this work, it is sampled with a 4 kHz clock using a dedicated field programmable gate array (FPGA) position sampling setup (PandABox, from Quantum Detectors<sup>12</sup>). For each clock period, the recorded photon counts from the photon detector (in this case, a photomultiplier tube) are also saved. The recorded information is streamed by transmission control protocol (TCP) to a control computer that processes the data. The PandABox FPGA configuration used in this work is shown in the Supplementary Information. The scanning of the sample is performed

by driving the piezoelectric stage amplifier using a trajectory generator implemented within the realtime kernel running the Orocosp library, whereas the requirements on the positioning feedback have been significantly relaxed compared to the PP and CV modes.

Table 1: Example of a datastream from the PandABox. Note that the table shows only a subset omitting other diagnostic information for simplicity.

$p_{M,x}$ [cts]	$p_{M,y}$ [cts]	Counts [cts]	Timestamp [s]
...	...	...	...
34858025	32360989	388513	107784.53560
34858028	32360996	389071	107784.53585
34858032	32361007	389616	107784.53610
34858024	32361005	390193	107784.53635
34858026	32361016	390757	107784.53660
34858027	32361033	391338	107784.53685
34858033	32361036	391913	107784.53710
34858041	32361043	392464	107784.53735
...	...	...	...

An example of the datastream transmitted by the PandABox is depicted in Tab. 1. The datastream contains two columns, where the  $x$  and  $y$  interferometer positions are recorded at the rising edge of the 4 kHz clock. The position is recorded in resolution units of the interferometer, which in our case corresponds to 150 pm/step. For experiments requiring 3D positioning, e.g. for tilted scans used to image in-plane magnetic systems,<sup>13</sup> or for laminography imaging,<sup>14</sup> a third column recording the  $z$  interferometer position can be added. The next column contains the photon counts detected during each clock cycle. This is done by connecting the total transistor logic (TTL) output of the photon discriminator unit (Hamamatsu C9744) to one of the digital logic inputs of the PandABox that is linked to a counter in the FPGA. The counter is enabled/reset at the start of the image and its value is polled at each clock cycle and transmitted into the datastream. The number of counts in each clock cycle has to be calculated by  $\Delta C(t) = C(t + 1) - C(t)$ . The final column is an absolute timestamp, expressed as seconds since the device was powered on.

The data stream is processed by a supporting computer, which performs the following calculations. First, the position values are converted from interferometer resolution units to

metric by multiplying them by the resolution of the interferometer ( $p_{R,(x,y)}(t) = p_{M(x,y)}(t) \times r_{(x,y)}$ , being  $r_{(x,y)} = 150$  pm in this case). As the interferometer position is recorded at the rising edge of the 4 kHz sampling clock, but the counts are recorded across the entire clock cycle, the position of the sample when these counts were acquired will be given by the average position between the current and the following rising edge of the sampling clock:

$$p_{(x,y)}(t) = \frac{p_{R,(x,y)}(t) + p_{R,(x,y)}(t+1)}{2},$$

For each of these calculated positions, the difference in the detector counts between the current and the following rising edge of the sampling clock will be assigned. Using the same example data shown in Tab. 1, the processed data will be as shown in Tab. 2.

Table 2: Example of a processed dataset. The rows are color-coded based on the pixel at which the data has been assigned (assuming a user-defined square binning size of 2 nm). Each row of the table corresponds to a sampling time of 250  $\mu$ s.

$p_x$ [ $\mu$ m]	$p_y$ [ $\mu$ m]	$\Delta$ Counts [cts]
...	...	...
5228.7040	4854.1489	558
5228.7045	4854.1502	545
5228.7042	4854.1509	577
5228.7038	4854.1516	564
5228.7040	4854.1537	581
5228.7045	4854.1552	575
5228.7056	4854.1559	551
...	...	...

Now, the processed data is binned according to a user-defined spatial bin dimension. All the recorded photon counts that fall within a given bin are summed up, and the total time interval which the position remained in the corresponding bin is recorded as well, as shown with the example data of Tab. 2 in Tab. 3. This provides a collection of recorded counts in a user-defined grid, i.e. an image. However, due to stochastic variations in the sample position, there is no guarantee that the time in which the sample position is inside a given bin is uniform across the entire ROI (the PP and CV must also suffer similar issues and the

most common strategy is to assume that the imperfections are not significant). Therefore, the recorded photon counts need to be normalized to the time interval of the defined bin, i.e. the per bin photon count rate needs to be displayed, as shown in Tab. 3. Note that the Poisson noise still needs to be calculated from the recorded photon counts.

Table 3: Example of a binned dataset using the same data as in Tab. 1. Each row of the table represents a pixel in the final reconstructed image, with the same color coding as in Tab. 2. Note here that, due to the fact that the pixels of the reconstructed image do not have the same dwell time, the quantity displayed will be the count rate, and not the total recorded counts. However, the Poisson noise is still determined by the total recorded counts.

Counts [cts]	Sample time [μs]	Count rate [Mcts/s]	Poisson noise [%]
...	...	...	...
558	250	2.232	4.23
1122	500	2.244	2.98
564	250	2.26	4.21
581	250	2.324	4.15
1126	500	2.252	2.98
...	...	...	...

The possibility to assign the recorded photon counts to the measured sample position allows for a correction of errors that arise from assuming a wrong sample position. This principle is shown in Fig. 3(b), where data points are assigned to different pixels depending on whether the data was acquired in CV mode (i.e. all data acquired within a dwell time is assigned to one pixel), or using the supersampled method, where the data is re-assigned to the correct pixel after the measurement.

To demonstrate the functionality and performance of the concept described above, we imaged a 10 nm Siemens star. This measurement is suited for demonstration of reduction of the imaging overhead, compensation of vibration effects and positioning glitches, and high-resolution imaging (< 10 nm pixel size). The Siemens star was fabricated at PSI with the line-doubling technique,<sup>15</sup> and consists of SiO<sub>2</sub> spokes coated with a 10 nm Ir layer, whereas the capping layer was removed after fabrication. At its center, the distance between two adjacent Ir layers is of approximately 11 nm. The Siemens star was imaged with two different FZPs. The first FZP, which was used for the vibration compensation proof-of-

concept measurement, is a 240  $\mu\text{m}$  diameter Au FZP with an outermost zone width of 35 nm. The second one, which was used for the proof-of-concept high-resolution imaging experiment, is a 240  $\mu\text{m}$  diameter Ir line-doubled FZP with an outermost zone width of 8.8 nm. Fabrication details of the high-resolution FZP can be found in.<sup>8,15</sup> For both FZPs, the secondary source of the PolLux beamline was closed sufficiently to guarantee a coherent illumination of the FZP that reaches the theoretical resolution limit of the X-ray lens. All of the Siemens star images shown below were acquired at a photon energy of 1 keV.

The overhead reduction was verified by performing the same image sequence shown in Fig. 2. For the supersampled imaging method, the images were performed in CV mode, reducing the ROI  $x$  dimension to account for the stage acceleration and deceleration distances (i.e.  $d = d_{\text{ROI}} - d_{\text{acc}} - d_{\text{decel}}$ ). With this method, a total overhead time of 10-15 % was achieved, independently of the desired pixel dwell time, and always lower than using either the PP or the CV modes (note here that the exact value of the overhead will still depend on parameters such as the number of lines in the image and the size of the ROI - but it will always be lowest with the supersampled imaging method). This is especially important at low dwell times, and will be of relevance for fast imaging experiments enabled by DLSRs, where the image overhead of the supersampled imaging method is significantly lower. Improvements on the positioning protocol may reduce this overhead further since precise timing of the pixel clock and precise positioning of the sample are not required for the supersampling method and only contribute to the controlled spread of applied photons across the imaged area.

The proof-of-concept vibration compensation measurement is shown in Fig. 4. In order to compare between the standard STXM imaging and the supersampled scanning microscopy method, an image was acquired in CV mode, while the same data was recorded in parallel using the PandABox. At half of the scan, a closed cycle cryostat cooler was switched on, generating significant mechanical vibrations that couple into the sample stage. Their effect are clearly visible in the standard CV STXM scan (Fig. 4(a)). In stark contrast, the sample vibrations can be completely mitigated with the supersampled method (Fig. 4(b)). Actually,

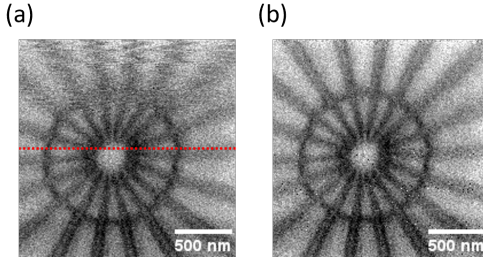


Figure 4: Proof-of-concept for vibration control. (a) STXM image acquired of a 10 nm Ir Siemens star acquired with the standard STXM setup. In the top half of the image, above the red line, a closed cycle cryostat cooler was turned on to demonstrate the effect of strong mechanical vibrations. (b) Same dataset as in (a), but reconstructed with the supersampling method. The reconstructed image shows no vibrations. Both images have a pixel size of 10 nm. Imaging performed with a 35 nm outermost zone FZP under diffraction-limited conditions. The effective dwell time is of 8 ms/px (Poisson noise of 1.3 %, compared to a contrast of 2.6 %).

strong sample vibrations have an advantageous side effect if scanning is performed in a line-at-once manner: high frequency vibrations enable a uniform sampling of the entire ROI, reducing variations in count rate errors (see the Supporting Information for additional details). Note, however, that only vibration modes where the distance between the sample and the interferometer mirror does not change can be compensated. High order vibration modes, and thermal drifts of the sample with respect to the interferometer mirror cannot be compensated in this way.

To demonstrate the high-resolution imaging, we acquired an image with the aim to resolve the 10 nm linewidth at the center of the Siemens star. Here, the imaging was performed by repeatedly scanning a  $900 \times 900$  nm $^2$  ROI around the center of the star following a meander pattern with a stage velocity of 5  $\mu$ m/s (CV scan with a nominal pixel size of 2.5 nm and a pixel dwell time of 0.5 ms). Due to the requirement of significantly narrowing down the secondary source size to guarantee coherent illumination conditions for the 8.8 nm outermost zone width FZP, a total pixel dwell time of about 38 ms was necessary to achieve the same ratio between contrast and Poisson noise (in practice, the ROI was scanned a total of 70 times until the necessary signal-to-noise ratio was reached). To provide a fair comparison between the standard STXM imaging and the supersampled imaging method, particular

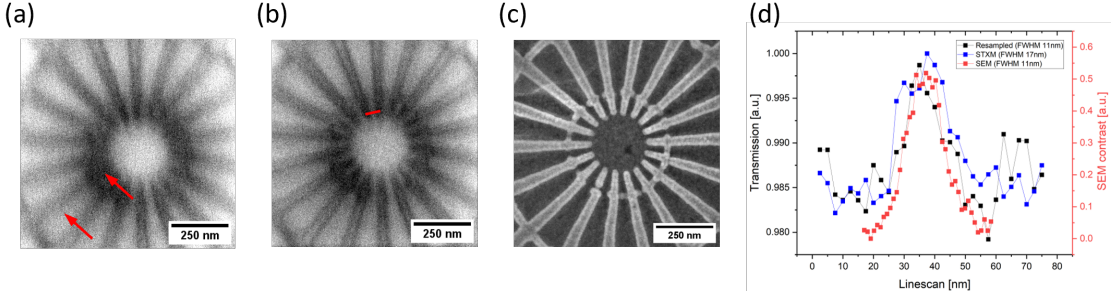


Figure 5: Proof-of-concept for high-resolution imaging. (a) High-resolution standard STXM image of the central area of a 10 nm Ir Siemens star. Several artifacts, marked by the red arrows, are visible in the image. A blur of the spokes in the vertical direction (caused by vibrations) is visible, and the center of the star cannot be fully resolved. (b) Same dataset as in (a), but evaluated from a supersampling stream. Using this method, the artifacts identified in (a) have been corrected, and the center of the star is well resolved. Both images have an effective pixel size of 2.5 nm. Imaging was performed with a 8.8 nm outermost zone FZP under diffraction-limited conditions. The effective dwell time is 38 ms/px (Poisson noise of 0.44 %, compared to a contrast of 2.6 %). (c) Scanning electron micrograph of the Siemens star imaged in (a-b). (d) Profile across the area marked in (b) derived from the standard STXM image, the supersampled reconstruction, and the SEM image. A significant reduction in the linewidth can be observed when using the supersampled reconstruction.

attention was dedicated to the minimization of environmental vibration sources and drift sources: we performed the scans at night time when environmental influences are minimal, and mounted the sample several hours before the measurement to provide enough settling time for thermal drifts and other related effects. Fig. 5(a) shows the resulting standard STXM image, where several imaging artifacts can be identified (marked by the red arrows in the figure). The marked artifacts (blur of the spokes and the insufficient spatial resolution in the center of the star along the  $x$  axis) are attributed to the vibration of the sample along the  $y$  axis (see Fig. 1(a)). When the same data set is evaluated using the supersampled method, the spokes appear sharp and the center of the star can be resolved uniformly (Fig. 5(b)), yielding an image with a quality that almost reaches the superior resolution of scanning electron microscopy (Fig. 5(c)). This becomes particularly evident when deriving profiles at the center of the star, shown in Fig. 5(d), where a clear difference between the standard CV STXM and the supersampled imaging can be observed.

Up to now, we demonstrated the correction of vibrations and scanning glitches, as well as

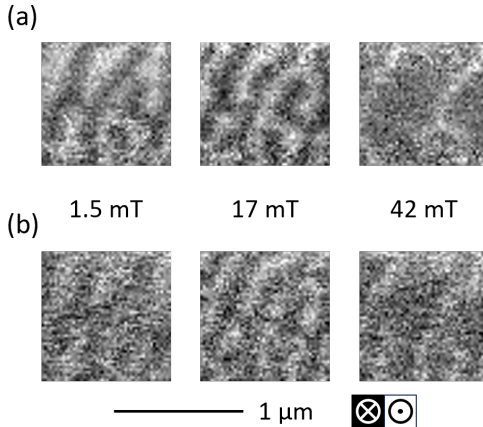


Figure 6: Single frames of a magnetic hysteresis loop in a SAF sample, cropped to a  $1 \times 1 \mu\text{m}^2$  area. (a) Acquisition performed using supersampled scanning microscopy. (b) Acquisition performed using standard CV STXM imaging. The direction of the magnetic contrast in the image (perpendicular magnetization) is indicated by the black/white bar. Each of the frames corresponds to a real time of 18 s. Effective pixel dwell time of 1.5 ms (Poisson noise of 1.5 %, compared to a contrast of 2.5 %). The full movie is shown in the Supporting Information.

the reduction of overhead times. As all three issues are particularly problematic for imaging at low pixel dwell times, STXM has not been significantly utilized in the past for the imaging of mesoscopic dynamical processes, i.e. processes occurring on time scales of seconds to minutes: the relatively slow scanning velocity would give rise to rolling shutter artifacts. By enabling fast imaging at low pixel dwell times whilst maintaining image fidelity, our method significantly reduces the impact of the rolling shutter artifact, allowing for the imaging of mesoscopic dynamical processes at the second/minute timescales. As a final proof-of-concept experiment, we recorded the magnetic hysteresis loop of a synthetic antiferromagnetic (SAF) multilayer superlattice, which is composed of 5 pairs of alternating layers of  $\text{Co}_{68}\text{B}_{32}$  and  $\text{Co}_{40}\text{Fe}_{40}\text{B}_{20}$  forming oppositely magnetized sublattices.<sup>16</sup> Thanks to the different Co content of the two layers, the magnetization of the  $\text{Co}_{68}\text{B}_{32}$  layer could be visualized by using circularly polarized X-rays tuned at the  $\text{L}_3$  edge of Co (ca. 778 eV), allowing us to employ the X-ray magnetic circular dichroism (XMCD) effect as contrast mechanism.<sup>16</sup> A 240  $\mu\text{m}$  diameter FZP with a 35 nm outermost zone width under coherent illumination conditions was utilized for this experiment.

An ROI of  $1.3 \times 1 \mu\text{m}^2$  was repeatedly scanned in a meander pattern with 50 lines ( $20 \text{ nm/line}$ ) at a stage velocity of  $10 \mu\text{m/s}$ . A single ROI frame scan requires approximately 7 s to complete. The ROI frame scan was repeated 300 times, and the position-dependent photon count rate was recorded as described above. During the acquisition of this scan, the out-of-plane magnetic field applied to the SAF film, generated by means of a rotatable permanent magnet installed above the sample, was continuously modified from 0 to 50 mT at a velocity of about 1 mT every 6 scanned frames (i.e.  $24 \mu\text{T/s}$ ). The recorded data was subdivided in 3 ROI-scans datasets. From each of them, an image of the magnetic configuration of the sample was reconstructed. This resulted in a 100 frame movie of the evolution of the magnetic state of the SAF film under an applied out-of-plane magnetic field from 0 to 50 mT with a 0.5 mT step/frame. A choice of recorded frames (the full movie is shown in the Supporting Information) is shown in Fig. 6(a), where they can be compared with the same frames acquired with the standard CV STXM setup (Fig. 6(b)). In the latter, several positioning artifacts can be observed. Each frame corresponds to a real time step of 18 s, giving a real time of 3 minutes for the movie. This timestep allows us to directly image (i.e. not stroboscopic imaging) dynamic processes occurring at the minute timescale, whilst maintaining a high image quality and fidelity. It has to be noted that the limiting factor for the timestep used in the recorded movie was not the velocity of the piezoelectric stage (a maximum stage velocity of  $300 \mu\text{m/s}$  can be achieved) but rather the acquired image statistics (i.e. Poisson noise-limited imaging). As PolLux is a bending magnet beamline, the photon flux at the detector is limited to about  $1 \text{ MPh/s}$ ,<sup>9</sup> which results in a Poisson noise of about 1.5 % for each of the frames shown in Fig. 6, compared to an XMCD contrast of about 2.5 % for this sample. Thanks to the significantly higher coherent photon flux delivered to the endstation,<sup>1</sup> an undulator-based beamline at a DLSR source will easily overcome this limitation, allowing for the acquisition of (non-reproducible) dynamics in the second and sub-second timescales. This is of interest for many applications, such as, e.g., the investigation of nucleation processes and phase transitions.<sup>17</sup>

In conclusion, we describe a new method for the acquisition of STXM images, called supersampled scanning microscopy. This concept is based on the measurement of the sample position and the detected photon counts at a high rate (faster than the mechanical vibrations), and subsequently binning of the data according to the recorded positions. An X-ray microscopy image can be obtained in this way, where positioning artifacts and mechanical vibrations are fully compensated. As additional advantages, the technique allows for a relaxation of the positioning precision in the scanning, significantly reducing imaging overheads if compared to the standard STXM PP and CV imaging protocols, whilst maintaining the possibility to acquire high-resolution images. Finally, the technique allows one to reduce the timescale of the rolling shutter artifact that is typical of scanning microscopy techniques, permitting the acquisition of mesoscopic dynamic movies at timescales limited by the available photon fluxes and scanning velocity of the piezoelectric stage. The performance of the technique was demonstrated by proof-of-concept experiments on the reduction of the imaging overhead, compensation of vibrations and positioning glitches, high-resolution imaging, and the acquisition of mesoscopic dynamic movies. This imaging protocol is currently being integrated into the Pixelator control system of the PolLux endstation,<sup>18</sup> including the possibility to perform live processing of the image. It will be made available for regular user operation. The position sampling frequency will also be increased to 10 kHz once live processing of the image is available (for the work presented here, we used a 4 kHz sampling rate to limit the amount of data generated per image).

As outlook for the technique, integration with time-of-arrival detection<sup>19</sup> would allow one to perform time-resolved pump-probe stroboscopic imaging without the requirement of PP positioning, once more reducing overhead times and resolution losses caused by vibrations. In this case, the PandABox and the time-to-digital converter used for the photon detection will have to be synchronized, in order to assign the recorded photon counts to the correct sample position. This can be done by feeding the 4 kHz sampling clock to one of the additional clock inputs of the time-to-digital converter, and synchronizing the start of the acquisition

by means of a TTL signal.

## Acknowledgement

This work was performed at the PolLux (X07DA) beamline of the Swiss Light Source, Paul Scherrer Institut, Villigen, Switzerland. The PolLux endstation was financed by the German Bundesministerium für Bildung und Forschung through contracts 05K16WED and 05K19WE2. This project was financed by the Swiss National Science Foundation under grant agreement No. CRSK-2\_227418. The authors thank Christopher Marrows for providing the SAF sample.

## References

- (1) Streun, A.; Garvey, T.; Rivkin, L.; Schlott, V.; Schmidt, T.; Willmott, P.; Wrulich, A. SLS-2 – the upgrade of the Swiss Light Source. *Journal of Synchrotron Radiation* **2018**, *25*, 631–641.
- (2) Raimondi, P.; et al. The extremely brilliant source storage ring of the european synchrotron radiation facility. *Communications Physics* **2023**, *6*, 82.
- (3) Butcher, T. A.; Finizio, S.; Heller, L.; Phillips, N. W.; Sarafimov, B.; Vaz, C. A. F.; Kleiber, A.; Watts, B.; Holler, M.; Raabe, J. Soft X-ray Ptychography with SOPHIE: Guide and Instrumentation. *Review of Scientific Instruments* **2025**, *96*, 123704.
- (4) Butcher, T. A.; Phillips, N. W.; Chei, C.-C.; Chang, S.-C.; Beinik, I.; Thånell, K.; Yang, J.-C.; Huang, S.-W.; Raabe, J.; Finizio, S. Imaging ferroelectric domains with soft X-ray ptychography at the oxygen K-edge. *Physical Review Applied* **2025**, *23*, L011002.

(5) Johansson, U. et al. NanoMAX: the hard X-ray nanoprobe beamline at the Max IV laboratory. *Journal of Synchrotron Radiation* **2021**, *28*, 1935.

(6) Walsh, C. L. et al. Imaging intact human organs with local resolution of cellular structures using hierarchical phase-contrast tomography. *Nature Methods* **2021**, *18*, 1532.

(7) Schneider, G. Zone plates with high efficiency in high orders of diffraction described by dynamical theory. *Applied Physics Letters* **1997**, *71*, 2242.

(8) Rösner, B. et al. Soft x-ray microscopy with 7 nm resolution. *Optica* **2020**, *7*, 1602–1608.

(9) Raabe, J.; Tzvetkov, G.; Flechsig, U.; Böge, M.; Jaggi, A.; Sarafimov, B.; Vernooij, M. G. C.; Huthwelker, T.; Ade, H.; Kilcoyne, D.; Tyliszczak, T.; Fink, R. H.; Quitmann, C. PolLux: a new facility for soft X-ray spectromicroscopy at the Swiss Light Source. *Review of Scientific Instruments* **2008**, *79*, 113704.

(10) Holler, M.; Raabe, J. Error motion compensating tracking interferometer for the position measurement of objects with rotational degree of freedom. *Optical Engineering* **2015**, *54*, 054101.

(11) Orocov Project documentation. <https://docs.orocos.org/>, Accessed: 2025-12-03.

(12) Zhang, S.; Abiven, Y. M.; Bisou, J.; Renaud, G.; Thibaux, G.; Ta, F.; Minolli, S.; Langlois, F.; Abbot, M.; Cobb, T.; Turner, J. C.; Uzun, I. S. PandABox: A Multipurpose Platform for Multi-technique Scanning and Feedback Applications. Proc. of International Conference on Accelerator and Large Experimental Control Systems (ICALEPCS'17), Barcelona, Spain, 8-13 October 2017. Geneva, Switzerland, 2018; pp 143–150, <https://doi.org/10.18429/JACoW-ICALEPCS2017-TUAPL05>.

(13) Finizio, S.; Wintz, S.; Kirk, E.; Suszka, A. K.; Wohlhüter, P.; Zeissler, K.; Raabe, J.

Control of the gyration dynamics of magnetic vortices by the magnetoelastic effect.  
*Physical Review B* **2017**, *96*, 054438.

(14) Witte, K.; Späth, A.; Finizio, S.; Donnelly, C.; Watts, B.; Sarafimov, B.; Odstrcil, M.; Guizar-Sicairos, M.; Holler, M.; Fink, R. H.; Raabe, J. From 2D STXM to 3D Imaging: Soft X-ray Laminography of Thin Specimens. *Nano Letters* **2020**, *20*, 1305–1314.

(15) Rösner, B.; Koch, F.; Döring, F.; Bosgra, J.; Guzenko, V. A.; Kirk, E.; Meyer, M.; na Ornelas, J. L.; Fink, R. H.; Stanescu, S.; Swaraj, S.; Belkhou, R.; Watts, B.; Raabe, J.; David, C. Exploiting atomic layer deposition for fabricating sub-10nm X-ray lenses. *Microelectronic Engineering* **2018**, *191*, 91.

(16) Barker, C. E. A.; Finizio, S.; Haltz, E.; Mayr, S.; Shepley, P. M.; Moore, T. A.; Burnell, G.; Raabe, J.; Marrows, C. H. Domain wall motion at low current density in a synthetic antiferromagnetic nanowire. *Journal of Physics D: Applied Physics* **2023**, *56*, 425002.

(17) Alpert, P. A.; Boucly, A.; Yang, S.; Yang, H.; Kilchhofer, K.; Luo, Z.; Padeste, C.; Finizio, S.; Ammann, M.; Watts, B. Ice nucleation imaged with X-ray spectromicroscopy. *Environmental Science: Atmospheres* **2022**, *2*, 335.

(18) Watts, B.; Finizio, S.; Witte, K.; Langer, M.; Mayr, S.; Wintz, S.; Sarafimov, B.; Raabe, J. Status of the PolLux STXM beamline. *Microscopy and Microanalysis* **2018**, *24*, 476.

(19) Finizio, S.; Mayr, S.; Raabe, J. Time-of-arrival detection for time-resolved scanning transmission X-ray microscopy imaging. *Journal of Synchrotron Radiation* **2020**, *27*, 1320.